RSC Advances

PAPER

View Article Online
View Journal | View Issue

Cite this: *RSC Adv.*, 2015, **5**, 42540

Carbon monolith with embedded mesopores and nanoparticles as a novel adsorbent for water treatment†

Long Chen,[a] Huaiyuan Wang,[b] Huige Wei,[c] Zhanhu Guo,[c] Mojammel A. Khan,[d] David P. Young[d] and Jiahua Zhu*[a]

Received 17th February 2015
Accepted 27th April 2015

DOI: 10.1039/c5ra03014e

www.rsc.org/advances

A novel carbon monolith material with embedded mesopores and nanoparticles has been synthesized *via* a facile catalytic graphitization process by using natural wood as the carbon precursor. BET results reveal a large specific surface area of 273.0 m^2 g^{-1} and a narrow pore size distribution, with pore diameters of ~4.0 nm. This unique material shows excellent toxic pollutants removal from water, including inorganic heavy metal ion (chromium(VI)) and organic dyes (methylene blue and methyl orange). Isothermal studies reveal its large removal capacities of 49.5, 61.7 and 68.2 mg g^{-1} for chromium(VI), methyl orange and methylene blue, respectively. Kinetic studies reveal that the removal process follows pseudo-second-order adsorption behavior. A mechanism study demonstrates that adsorption, electrostatic interaction and a redox reaction are involved in the pollutant removal process, and contribute to the large adsorption capacities and excellent rate performance. The widely accessible natural resources, low cost, convenient fabrication, and superior adsorption properties would facilitate this new material promising applications in the fields of water pollutant control and purification.

Introduction

A shortage of clean drinking water has become an unavoidable worldwide issue nowadays. The toxic pollutants (organic, inorganic and biological) existing in both the natural water supply and industrial wastewater streams pose great risks to human health and the environment. With increasing concerns about clean environment and human health, technologies with high efficiency and low cost to reduce the pollutant content in wastewater are in urgent demand. Pollutants in water can be roughly divided into three main categories: organics, inorganics and pathogens. Typical polluted water contains multiple contaminants from a single category or different categories. Most of the current research deals with contaminants in a single category, while advanced technologies that are capable of handling contaminants from multiple categories are in demand to make the process more efficient.

Different water treatment processes, physical,[1–3] chemical,[4–7] and biological,[8,9] have been developed to remove organic and inorganic pollutants from wastewater. Among all the technologies developed, adsorption is the most applied technology since it can produce high quality water through economically feasible processes. Depending on the nature of the interaction between adsorbent and adsorbate, adsorption can be described as physisorption, chemisorption or electrostatic interaction. Physisorption depends on van der Waals forces, and chemisorption is based on covalent bonding. Factors influencing the adsorption behaviour of an adsorbent generally include particle size, surface area of adsorbent, affinity of adsorbate to solvent and adsorbent, adsorbent size with respect to pore size, surface charge, pH *etc.*[10] Though activated carbon is a well-accepted adsorbent, the relatively high manufacturing cost is still the major obstacle that limits its wider applications. Therefore, tremendous research efforts have been devoted to developing new adsorbents with better efficiency and significantly reduced cost.[11–13]

Recently, magnetic nanoparticles have been found to be efficient adsorbents with the unprecedented advantages of large specific surface area, small diffusion resistance, and fast and complete reactions.[14,15] In addition, magnetic separation by an external magnetic field provides a feasible route for online separation of the magnetic nanoparticles from the homogeneous solution. However, the serious aggregation of nanoparticles is often inevitable and results in low durability at long term operation. Therefore, hybrid nanocomposites embedding magnetic

[a]*Intelligent Composites Laboratory, Department of Chemical and Biomolecular Engineering, The University of Akron, Akron, OH 44325, USA. E-mail: jzhu1@uakron.edu; Tel: +1 330 972 6859*

[b]*College of Chemistry and Chemical Engineering, Northeast Petroleum University, Daqing 163318, P. R. China*

[c]*Dan F. Smith Department of Chemical Engineering, Lamar University, Beaumont, TX 77710, USA*

[d]*Department of Physics and Astronomy, Louisiana State University, Baton Rouge, LA 70803, USA*

† Electronic supplementary information (ESI) available: Experimental details and additional characterization data. See DOI: 10.1039/c5ra03014e

nanoparticles on/in suitable substrates have been developed to improve the dispersibility and thus enhance the pollutant removal efficiency. A wide range of supporting substrates has been used, including clay,[16] polymer,[17] metal oxide,[18] biomolecules[19] and carbon (activated carbon,[20] mesoporous carbon,[21–24] carbon nanotubes,[25] and graphene[26,27]). For example, bentonite-supported nanoscale zero-valent iron (B-nZVI)[16] was demonstrated to be more effective than nZVI in Cr(VI), Pb(II), Cu(II) and Zn(II) removal from electroplating waste water. In addition, other similar magnetic nanocomposites such as Fe_3O_4 coated polypyrrole,[17] hierarchical Fe_3O_4/MnO_2,[18] Fe_3O_4/chitosan,[19] Fe/activated carbon[20] and $Fe@Fe_2O_3@Si–S–O$/graphene,[26] have been reported as efficient adsorbents for Cr(VI) removal. Meanwhile, magnetic nanocomposites (Fe_3O_4/MWCNTs,[25] Fe_3O_4/layered double hydroxide,[28] Fe_3O_4/graphite oxide,[29] Fe_3O_4/graphene[30,31] and Fe/carbon[32]) were found effective in organic pollutant removal.

Even though tremendous research efforts have been devoted to design hybrid adsorbents, less work has been done to control the pore structure of magnetic nanocomposites, which is actually the key factor in fully exploring the advantages of nanoscale materials in practical applications. Currently, the most widely-employed techniques for manufacturing porous carbon nanostructures mainly rely on the template method, using either hard-[33–35] or soft-templates.[36–38] However, the template approaches usually suffer from high cost, complicated operations and environmental pollution induced during the template removal process. Alternative technologies to fabricate magnetic nanocomposites with well-controlled porous structures and significantly reduced manufacturing costs are in urgent demand.

In this work, natural wood was selected as the carbon precursor to synthesize a mesoporous magnetic carbon nanocomposite *via* a facile catalytic graphitization process without using surfactants/templates. The microstructure of the resulting nanocomposite was carefully characterized by various techniques including SEM, HRTEM, XRD, TGA and BET. The isotherm and kinetic adsorption tests for inorganic Cr(VI) and organic dyes (methylene blue and methyl orange) were performed to investigate the adsorption capacities and adsorption rates of the nanocomposite. The mechanism for pollutant removal and the reusability of the adsorbent were also investigated.

Experimental

Materials

Potassium dichromate ($K_2Cr_2O_7$, 99%), 1,5-diphenyl carbazide (DPC), methylene blue (MB), and methyl orange (MO) were purchased from Fisher Scientific. Phosphoric acid (85 wt%), ethanol and iron nitrate (>98%) were purchased from Sigma-Aldrich. All the chemicals were used as received without further treatment. Natural wood was chosen as the source material to fabricate the carbon nanocomposite. To ensure complete soaking, the wood block was chopped into small chunks ($3 \times 3 \times 10$ mm) before soaking in 1.0 M $Fe(NO_3)_3$ solution. In addition, the soaking process was performed in a vacuum oven (0.09 MPa) overnight at room temperature. It is worth mentioning that the central area of the chunk cannot be completely soaked without a vacuum even with an elongated soaking time. The soaked brownish wood chunk was then dried at room temperature for two days and then annealed at 800 °C for two hours in nitrogen with a heating rate of 10 °C min^{-1}. After cooling down to room temperature, the product (c-WFe) was collected for characterization and further pollutant removal tests. For comparison, natural wood was also carbonized (c-Wood) following the same annealing procedure to obtain porous carbon materials for pollutant removal testing.

Testing methods

Standard curves relating the contaminant concentration and UV-Vis peak intensity at certain wavelengths (Cr(VI) at 540 nm after coloration, MB at 663 nm, MO at 465 nm) were constructed to measure the pollutants' concentrations. Aqueous Cr(VI) solutions with different concentrations (200, 400, 600, 800 and 1000 ppb) were treated with 2.0 g L^{-1} c-Wood and c-WFe to study the effect on the Cr(VI) concentration. For the adsorbent concentration study, the Cr(VI) with a fixed concentration of 500 ppb was treated with different concentrations of c-Wood and c-WFe (0.5, 1.0, 2.0 and 3.0 g L^{-1}). The adsorption test was performed at room temperature for a 15 min period. The adsorbent was immediately separated from the solution by centrifugation. The residual solutions were then collected and subjected to colorimetric analysis (for details refer to ESI S1†) to determine the remaining Cr(VI) concentrations. The study on MB and MO adsorption used higher adsorbate concentrations of 25, 50, 75, 100 and 125 ppm but the same adsorbent dosage of 2.0 g L^{-1} c-Wood and c-WFe. To study the influence of adsorbent dosage, 1.0, 1.5, 2.0 and 3.0 g L^{-1} c-Wood or c-WFe were used for adsorption with 10.0 mL 50 ppm MB (or MO) solution for 30 min. Adsorption isotherms of c-Wood and c-WFe with Cr(VI), MB and MO were obtained to determine the adsorption capacities. During the tests, a fixed amount of adsorbents (0.005 g) were mixed with pollutant solutions (10 mL) of different initial concentrations and the mixtures were stirred for 12 hours to ensure that equilibrium was reached. The remaining pollutants in water were determined with UV-Vis and the adsorbed quantity was calculated to quantify the adsorption capacity. The adsorption kinetic study was performed by using 2.0 g L^{-1} c-WFe in 50 mL contaminant solutions (Cr(VI): 1000 ppb, MB: 50 ppm, and MO: 100 ppm) with sampling times of 1, 3, 5, 7, 10, 15 and 30 min. Tests were performed at three different temperatures, 20 °C, 40 °C and 60 °C, for each contaminant.

Characterization

The morphologies of c-Wood and c-WFe were characterized by scanning electron microscopy (SEM, JEOL-7401). The statistical analysis of the SEM images was performed with ImageJ software. c-WFe was further characterized by high resolution TEM FEI (Tecnai G2 F20). Each TEM sample was prepared by drying a drop of sample powder ethanol suspension on a carbon-coated copper TEM grid. The crystalline structures of c-Wood and c-WFe were examined by X-ray diffraction (XRD, Rigaku, Ultima

IV). The Raman spectra of c-Wood and c-WFe were characterized with a Horiba LabRam HR Micro Raman Spectrometer within the range of 400–3000 cm^{-1}. Metal nanoparticle loading in c-WFe was determined by thermogravimetric analysis (TGA, TA Q500) in air from 20 to 800 °C with a 10 °C min^{-1} heating rate. Specific surface areas and pore-size distributions were measured by N_2 adsorption at 77.4 K with a Quantachrome Nova 2200e. Prior to each measurement, samples were degassed at 300 °C for 12 h under high vacuum (<0.01 mbar). The pore size distribution was calculated by the Barrett–Joyner–Halenda (BJH) method using desorption isotherms. The surface potential of c-Wood and c-WFe in neutral deionized water were measured using a Zetasizer Nano-ZS90 (Malvern). To quantify the concentration of iron ions that leached into the polluted water during adsorption, inductively coupled plasma (ICP) analysis was performed on an ICP-OES unit (Perkin Elmer P-400). The magnetic properties of the c-WFe before and after adsorption tests were measured in a 9 T physical properties measurement system (PPMS) by Quantum Design.

Results and discussion

The morphologies of the c-Wood and c-WFe were examined by SEM. The side views of both samples show a clear laminar structure, Fig. 1(a) and (c). A closer look at the c-WFe shows that the nanoparticles (white dots) are densely distributed on the carbon surface, inset of Fig. 1(c). The average particle size is measured to be about 100 nm with a narrow size distribution. Fig. 1(b) and (d) exhibit the top views of the cross sections of c-Wood and c-WFe, and show predominantly ordered quadrilateral and pentagonal tubular structures. The tube area of c-Wood distributes in a wide range of 100–800 μm^2 with an average of 324.1 μm^2. A smaller average tube area size of 250.0 μm^2 is obtained in c-WFe with a narrower distribution in the range 100–500 μm^2. The smaller average tube area in c-WFe is predominantly attributed to the catalytic graphitization where the carbon lattice tends to arrange in an ordered and tightly packed structure. This has been further confirmed in the following HRTEM and XRD study.

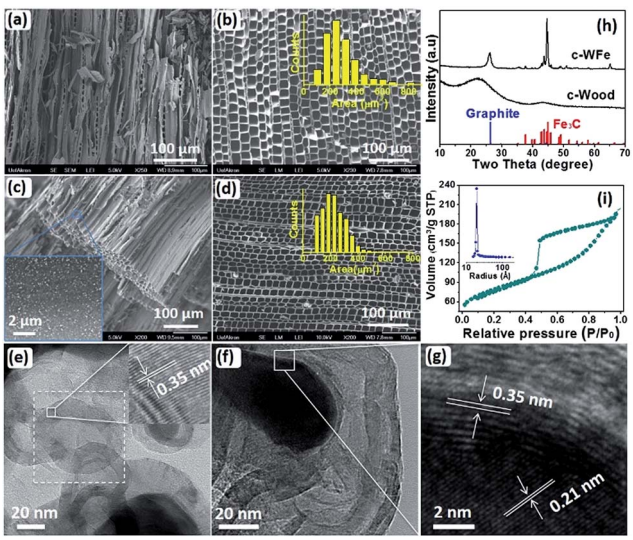

Fig. 1 SEM of c-Wood: (a) side view, (b) top view; inset shows the statistical distribution of pore area. SEM of c-WFe: (c) side view; inset figure shows the nanoparticle distribution on the side wall, (d) top-view and pore area distribution of cross-section of c-WFe. HRTEM of c-WFe focusing on (e) carbon; inset figure clearly indicates the graphitized carbon with a lattice fringe of 0.35 nm, (f) NPs/carbon interface, and (g) enlarged interface of (f) showing lattice fringes of iron carbide (0.21 nm) and graphitized carbon (0.35 nm). (h) XRD pattern of c-Wood and c-WFe. (i) Nitrogen adsorption isotherm of c-WFe at 77.4 K, and the pore size distribution.

Besides the micrometer-sized hollow tube structure, nanometer-sized pores are also observed in the tube wall of c-WFe. Fig. 1(e) shows hollow carbon spheres with graphitized carbon shells. The inset figure shows an enlarged area and the lattice spacing is measured as 0.35 nm corresponding to graphite. The nanoparticles are not observed in the area enclosed by the dashed square, which indicates that carbon graphitization does not necessarily occur locally on the nanoparticle surface. In fact, the nanoparticles will be liquefied during annealing and move freely on the carbon substrate that converts amorphous carbon to graphitized carbon along its flow path.[39] The nanoparticles tend to aggregate with each other to minimize their surface energy and the irregular flowing pattern results in a wide particle size distribution from 5 to 200 nm, Fig. S1.† Taking a closer look at the nanoparticle/carbon interface, the lattice fringes of iron carbide (0.21 nm) and graphitized carbon (0.35 nm) can be clearly identified, Fig. 1(f) and (g). Fig. 1(h) shows the XRD patterns of both c-Wood and c-WFe. The peak at $2\theta = 26.2°$ in c-WFe corresponds to the (002) crystal plane of graphite carbon.[40,41] Comparing this peak to the broad peak at the lower angle position in c-Wood, the catalytic graphitization of iron in c-WFe could be verified, and this is consistent with previous literature reports.[21,42,43] The major peaks of c-WFe between 35 and 70° are indexed to the crystalline planes of Fe_3C (PDF#35-0772). The graphitization degree of the carbon in c-WFe can be calculated using the Mering–Maire eqn (1):[44]

$$g = \frac{0.3440 - d_{002}}{0.3440 - 0.3354} \quad (1)$$

where g is the graphitization degree, 0.3440 is the lattice spacing of non-graphitized carbon and 0.3354 is the lattice spacing of 100% graphitized carbon. From the carbon (002) crystal plane with $2\theta = 26.2°$, d_{002} is calculated as 0.3398 nm by using the Bragg eqn (2):

$$2d_{002}\sin\theta = n\lambda \quad (2)$$

where d_{002} is the atomic lattice spacing of carbon, $\theta = 13.1°$ is the angle between the incident ray and the scattering planes, $n = 1$ is an integer, and $\lambda = 1.54056$ Å is the wavelength of the incident wave. The graphitization degree in c-WFe is calculated as 46.7%. Raman results confirm the larger proportion of graphitized carbon in c-WFe, Fig. S2.† The carbon yields are 27.45% and 37.48% in c-Wood and c-WFe, respectively, ESI S4.†

A nitrogen adsorption–desorption isotherm was obtained at 77.4 K to confirm the existence of mesopores in the tube walls of c-WFe, Fig. 1(i). The isotherm is a typical type-IV curve, which

clearly indicates the formation of mesopores in c-WFe.[45,46] The adsorption–desorption of c-Wood cannot be completed due to its very low surface area. In c-WFe, the introduced nanoparticles promote the catalytic graphitization of the surrounding carbon, and void space is created between the nanoparticles due to the non-uniform structural shrinkage during annealing. The inset figure reveals a very narrow pore size distribution with a pore radius of ~20 Å. c-WFe shows a large specific surface area of 273.0 $m^2\ g^{-1}$ with a pore volume of 0.32 $cm^3\ g^{-1}$ at a relative pressure of 0.986. From TGA in Fig. S4,† the loading of Fe_2O_3 is determined to be 35.9 wt% in c-WFe, which corresponds to 25.1 wt% of iron. By excluding the mass fraction of iron, the specific surface area of the porous carbon in c-WFe is calculated as 364.5 $m^2\ g^{-1}$.

To precisely quantify the pollutant concentration, standard curves have been constructed relating pollutant concentrations to UV-Vis peak intensity at specific wavelengths, Fig. S5–S7.† Highly linear standard curves are obtained for Cr(VI), MB and MO with correlation factors (R^2) of greater than 0.99, Fig. 2(a). The pollutant concentration effect on the removal percentage was studied with 2.0 g L^{-1} c-WFe, Fig. 2(b). The results indicate that the Cr(VI) can be completely removed at concentrations <400 ppb. When the initial Cr(VI) concentration is increased to 1000 ppb, the removal percentage decreases to about 85%. This is because the active sites eventually become saturated with adsorbed Cr(VI), at which point further addition of Cr(VI) hardly increases the amount of adsorbed Cr(VI). Much higher adsorption capacities for organic dyes have been observed in c-WFe, where >20 ppm levels of both MB and MO have been removed with a similar loading of c-WFe. Thus the effect of c-WFe concentration on removal percentage was studied with 500 ppb Cr(VI) and 50 ppm dye at varied c-WFe concentrations of 0.5, 1.0, 2.0 and 3.0 g L^{-1}, Fig. 2(c). Complete removal of both dyes

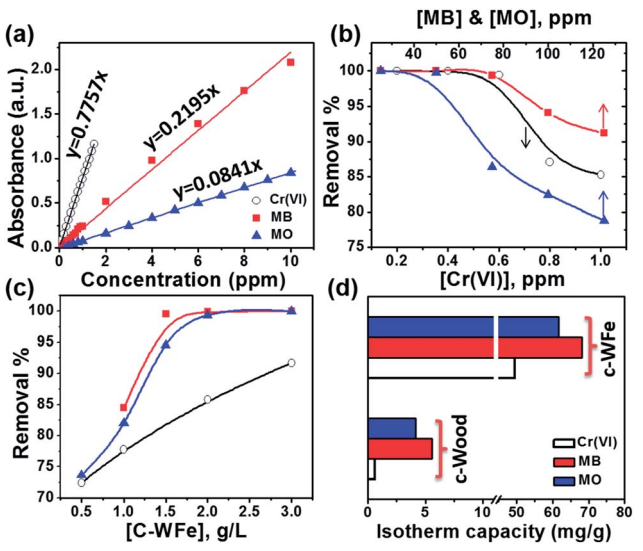

Fig. 2 (a) Standard curves of Cr(VI), MB, and MO relating pollutant concentrations with UV-Vis peak intensity at 540, 663 and 465 nm, respectively, R^2 > 0.99. Effect of (b) pollutant concentration and (c) adsorbent concentration on removal percentage. (d) Isotherm adsorption capacities of c-Wood and c-WFe with Cr(VI), MB and MO.

can be achieved with 2.0 g L^{-1} c-WFe while only ~90% removal of Cr(VI) was observed even with 3.0 g L^{-1} c-WFe. The effective removal of both a cationic dye (MB) and an anionic dye (MO) indicates that electrostatic interaction is not the dominating factor for the observed large adsorption capacities. However, the surface charge on the adsorbent surface affects the dynamic motion of ions towards the adsorbent surface *via* electrostatic forces, which largely depend on the charge pairing (same charge or opposite charge) between adsorbent and ions. This electrostatic force is found as the dominant factor that affects the adsorption rate in the following kinetic study.

Isotherm adsorption studies were performed at room temperature for 12 hours to quantify the maximum adsorption capacities (q_{max}) of c-WFe in association with the three pollutants. Similar tests were also performed on c-Wood for proper comparison. By fitting the isotherm adsorption results with the Langmuir model, as presented in eqn (3), the maximum adsorption capacity can be quantified:

$$\frac{C_e}{q_e} = \frac{C_e}{q_{max}} + \frac{1}{q_{max}k} \quad (3)$$

where C_e is pollutant concentration in the remaining solution (mg L^{-1}) at equilibrium, q_{max} is the maximum adsorption capacity (mg g^{-1}) of adsorbent and k represents the energy constant related to the energy of adsorption. q_e is the amount of pollutant adsorbed onto adsorbent (mg g^{-1}) at equilibrium and can be calculated by eqn (4):

$$q_e = \frac{C_0 - C_e}{m} \times V \quad (4)$$

where C_0 and C_e are initial and equilibrium concentrations of pollutant (mg L^{-1}), m is the adsorbent mass in g and V is the solution volume in L. q_{max} and k can be determined from the slope and intercept in a linear fitted $C_e/q_e \sim C_e$ plot. As determined from the Langmuir model, the q_{max} values of c-WFe (~50–70 mg g^{-1}) for all three pollutants are more than 10 times higher than those of c-Wood (<1 mg g^{-1} for Cr(VI); ~5 mg g^{-1} for MB and MO), Fig. 2(d). The larger adsorption capacities of c-WFe are predominantly due to the created mesoporous structure that provides a much larger effective surface area for pollutant adsorption. Meanwhile, the embedded nanoparticles with exposed surfaces react with pollutants and contribute to the enhanced adsorption capacities. In particular, the q_{max} = 49.5 mg g^{-1} for Cr(VI) adsorption is much larger than most of the q_{max} values in the literature reports (pomegranate husk carbon: 35.2 mg g^{-1};[47] carbon coated magnetic nanoparticles: 1.5 mg g^{-1};[48] graphene nanocomposites: 1.0 mg g^{-1};[26] 3D flower-like CeO_2: 5.9 mg g^{-1};[49] rice husk ash: 25.6 mg g^{-1} (ref. 50)).

Kinetic studies were performed at different temperatures, 20, 40 and 60 °C, with fixed [c-WFe] = 2.0 g L^{-1} and pollutants at specified concentrations ([Cr(VI)] = 1000 ppb, [MB] = 50 ppm, [MO] = 100 ppm). It is obvious that higher removal percentages were achieved with increasing solution temperatures. For example, 90% of the Cr(VI) could be removed at 20 °C with an adsorption time of 30 min, while 100% removal was achieved at 60 °C with a significantly shortened time period of 7 min,

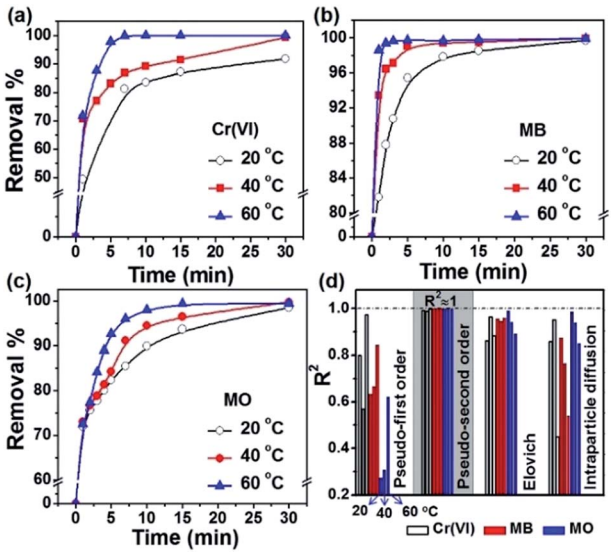

Fig. 3 Kinetic adsorption of (a) Cr(VI), (b) MB and (c) MO by c-WFe at 20, 40 and 60 °C. [Cr(VI)] = 1000 ppb, [MB] = 50 ppm, [MO] = 100 ppm and [c-WFe] = 2.0 g L^{-1}. (d) Plot of correlation factor R^2 by fitting kinetic results with four different models.

Fig. 3(a). A similar phenomenon was also observed for MB and MO, Fig. 3(b) and (c).

These kinetic results were then fitted with different kinetic models including pseudo-first-order, pseudo-second order,[21,51] Elovich,[52,53] and intraparticle diffusion.[54] The formulas and parameters of the four kinetic models are provided in Table S1.† The correlation coefficient (R^2) is used to evaluate the suitability of each model. A higher R^2 value indicates a more applicable model. Fig. 3(d) summarizes the R^2 results obtained from the four different models by fitting the kinetic results at different temperatures. Among these models, the pseudo-second order acquires the highest R^2 for each pollutant at different temperatures. Specifically, the pseudo-second order kinetics can be expressed in eqn (5):

$$\frac{t}{q_t} = \frac{1}{k_{ad}q_e^2} + \frac{t}{q_e} \quad (5)$$

where q_t (mg g^{-1}) is the solid-phase loading of pollutant in the c-WFe at time t (min.), q_e (mg g^{-1}) is the adsorption capacity at equilibrium and k_{ad} (g mg^{-1} min^{-1}) is the rate constant of adsorption. h (mg g^{-1} min^{-1}) is the initial adsorption rate at t approaching zero, $h = k_{ad}q_e^2$.

The regression results from the pseudo-second order kinetic model are summarized in Table 1. Apparently, the equilibrium adsorption capacity (q_e) is less dependent on the adsorption temperature since the adsorbent surface has not reached saturation within a short adsorption time, but temperature affects the adsorption rate significantly especially for the organic pollutants. The much larger adsorption rate constant (k_{ad} > 1.5 g mg^{-1} min^{-1}) of c-WFe compared to other currently used materials (typically, k_{ad} < 0.5 g mg^{-1} min^{-1} (ref. 47 and 55)) provides an unprecedented advantage in fast Cr(VI) removal. Moreover, c-WFe exhibits much larger q_e values in organic pollutant adsorption (for both MB and MO), which reach 25.64 mg g^{-1} and 50.25 mg g^{-1} at 20 °C, respectively. All three pollutants show increasing adsorption rate constants K_{ad} with increasing temperature due to the accelerated diffusion of pollutants at elevated temperature. A much higher rate constant is observed for Cr(VI) followed by MB and MO. The adsorption rate is mainly determined by the adsorbent/adsorbate interaction, which includes physisorption, chemisorption and electrostatic forces. The smaller ion size of Cr(VI) allows its faster diffusion into the internal pore area of c-WFe and thus the highest rate constant was observed for Cr(VI). With regard to the relatively larger MB and MO molecules, slower diffusion is expected and electrostatic forces at the adsorbent/adsorbate interface play an important role. The surface charge of both c-Wood and c-WFe were measured as −36.7 and −48.5 mV in neutral aqueous solution, indicating that both materials are negatively charged on the surface. When cationic MB molecules encounter negatively charged c-WFe, positive/negative charge attraction dominates the interfacial interaction behavior. When anodic MO approaches the c-WFe surface, charge repulsion dominates the interfacial interaction and results in a significantly lower rate constant than that of MB.

To reveal the pollutant removal mechanism, c-WFe was characterized by XRD before and after adsorption treatment to monitor the crystalline structure changes during the process. Fig. 4(a) shows the XRD pattern of the original c-WFe, and its XRD patterns after treatment with Cr(VI), MB and MO (Fig. 4(a), II–IV, respectively). Compared to the original c-WFe, the peak intensity ratio of Fe_3C (44.7°)/C (26.1°) decreased from 2.92 to 2.44, 2.08 and 2.34 after treatment with Cr(VI), MB and MO respectively. These results indicate that not only physisorption (the adsorbed MB and MO on the c-WFe surface can be easily washed out by ethanol, demonstrated in Fig. S15†), but also redox reactions are involved in the pollutant removal process. The smaller I(Fe_3C)/I(C) ratio

Table 1 Regression results from the pseudo-second order kinetic model

	Parameter								
	q_e (mg g^{-1})			K_{ad} (g mg^{-1} min^{-1})			h (mg g^{-1} min^{-1})		
Species	20 °C	40 °C	60 °C	20 °C	40 °C	60 °C	20 °C	40 °C	60 °C
Cr(VI)	0.48	0.51	0.51	1.57	1.91	7.63	0.36	0.49	1.96
MB	25.64	25.64	25.00	0.14	0.51	2.69	90.91	333.33	1683.50
MO	50.25	51.02	50.76	0.022	0.024	0.04	54.64	63.29	106.16

indicates the decreased weight fraction of Fe_3C species in the sample. The decrease in Fe_3C is due to its oxidization and dissolution in water as oxidized Fe^{2+} or Fe^{3+} ion forms. To verify the redox reaction, the Fe ion concentration in polluted water was continuously monitored with the ICP technique, Fig. 4(b). Generally, the MB adsorption releases the highest concentration of Fe ions (up to 1.1 ppm) and is followed by MO and Cr(VI). These observations are highly consistent with the XRD results, where the decrease in the $I(Fe_3C)/I(C)$ ratio follows the same MB > MO > Cr(VI) pattern, clearly indicating the extent of Fe dissolution from c-WFe. It is worth mentioning that the Fe ion concentration experienced a sharp increase during the initial few hours and then decreased to a lower level when exposed to MB and MO solution. This phenomenon suggests that a redox reaction occurs initially, accompanied with a fast release of Fe ions. After that, Fe ion adsorption back onto the c-WFe adsorbent becomes dominant as the reaction slows down. The Fe ion concentration remains at a low level in Cr(VI) water, indicating the negligible involvement of redox reactions in that case. The dissolution of elemental Fe from c-WFe is also reflected in the magnetization loss, Fig. 4(c). The larger magnetization loss indicates the more dissolved Fe. The saturation magnetization of c-WFe at 20 000 Oe decreases from 37.4 to 36.8, 36.6 and 35.8 emu g^{-1} after adsorption with Cr(VI), MO and MB, respectively. All these results reveal that the redox reaction is involved in the pollutant removal process, but adsorption is still most likely to be the dominating process.

Since MB adsorption presents the lowest $I(Fe_3C)/I(C)$ value indicating the largest portion of involved redox reactions, typical cycle tests were then performed on MB as shown in Fig. 4(d). It is revealed that the adsorption capacity of c-WFe decreased by ~50% during the initial three cycles and then stabilized at 50% until the 5th cycle. The capacity loss during the initial three cycles could be attributed to the oxidation of Fe_3C. Once the exposed Fe_3C has been fully consumed, the adsorption capacity only relies on the intrinsic surface area where no surface composition change occurs with increasing cycle number. This also explains the stabilized adsorption retention at ~50% after the first three cycles.

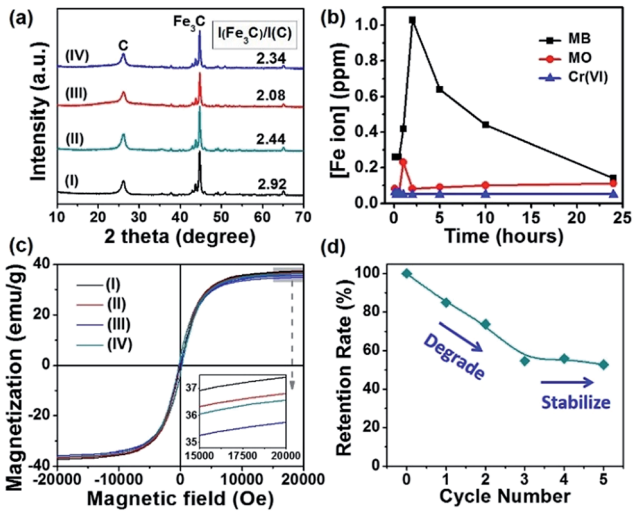

Fig. 4 (a) XRD pattern of c-WFe (I) as-synthesized, and after treatment with (II) Cr(VI), (III) MB, and (IV) MO. (b) ICP results of Fe ions in water with adsorption times up to 24 hours. [MB, MO and Cr(VI)] = 100 ppm, [c-WFe] = 1.0 g L^{-1}. (c) Magnetic properties of c-WFe before and after treatment, [c-WFe] = 1.0 g L^{-1}, [MB, MO and Cr(VI)] = 100 ppm, adsorption time: 12 hours. (d) Retention rate of c-WFe in removing MB during the first 5 cycles.

Conclusion

A facile process to manufacture mesoporous carbon nanocomposites from natural wood has been developed, which involves impregnation with an aqueous iron precursor and subsequent annealing (catalytic graphitization) in an inert atmosphere. The iron precursor converted to iron nanoparticles during annealing and served as a catalyst, transforming wood to graphitized carbon. The graphitization induced non-uniform shrinkage surrounding the catalyst creates a uniform mesoporous structure within the composite. Together with the natural monolith structure of the wood, this composite shows a micro-tubular/mesopore hybrid structure. This unique structure provides sufficient surface area for toxic species adsorption from polluted water and superior removal of Cr(VI), MB and MO were demonstrated. Besides, the decorated iron nanoparticles served as active sites to react with the pollutant species. Adsorption, electrostatic attraction and redox reaction were revealed as the major mechanisms for the fast pollutant removal. A kinetic study revealed the ultrafast rate constant of the adsorption process that required only minutes to achieve complete removal. This facile synthetic method provides a template-free approach to fabricate hierarchical mesoporous nanocomposites, which can be easily extended to synthesize other mesoporous materials. Deriving from natural resources, these materials are expected to receive significant attention in practical water treatment applications and other related areas such as energy storage and catalysis.

Acknowledgements

This work is financially supported by the start-up fund of The University of Akron. Partial support from the Faculty Research Committee, Biomimicry Research Incentive Center and a Firestone Faculty Research Fellowship from The University of Akron are also acknowledged. DPY acknowledges support from the NSF under Grant no. DMR1306392. HRTEM was performed at the Liquid Crystal Institute, Kent State University supported by the Ohio Research Scholars Program Research Cluster on Surfaces in Advanced Materials. The authors appreciate the technical support from Dr Min Gao with HRTEM.

References

1 A. Afkhami and R. Moosavi, *J. Hazard. Mater.*, 2010, **174**, 398–403.
2 Z. Geng, Y. Lin, X. Yu, Q. Shen, L. Ma, Z. Li, N. Pan and X. Wang, *J. Mater. Chem.*, 2012, **22**, 3527–3535.

3 J. Yang, J.-X. Wu, Q.-F. Lü and T.-T. Lin, *ACS Sustainable Chem. Eng.*, 2014, **2**, 1203–1211.
4 N. Kongsricharoern and C. Polprasert, *Water Sci. Technol.*, 1996, **34**, 109–116.
5 S. Rengaraj, C. K. Joo, Y. Kim and J. Yi, *J. Hazard. Mater.*, 2003, **102**, 257–275.
6 S. Rengaraj, K.-H. Yeon and S.-H. Moon, *J. Hazard. Mater.*, 2001, **87**, 273–287.
7 X. Zhu, J. Ni, J. Wei, X. Xing and H. Li, *J. Hazard. Mater.*, 2011, **189**, 127–133.
8 S. M. d. A. G. U. de Souza, K. A. S. Bonilla and A. A. U. de Souza, *J. Hazard. Mater.*, 2010, **179**, 35–42.
9 I. K. Kapdan and R. Ozturk, *J. Hazard. Mater.*, 2005, **123**, 217–222.
10 A. Dąbrowski, P. Podkościelny, Z. Hubicki and M. Barczak, *Chemosphere*, 2005, **58**, 1049–1070.
11 L. C. Hsu, S. L. Wang, Y. C. Lin, M. K. Wang, P. N. Chiang, J. C. Liu, W. H. Kuan, C. C. Chen and Y. M. Tzou, *Environ. Sci. Technol.*, 2010, **44**, 6202–6208.
12 Z. Ai, Y. Cheng, L. Zhang and J. Qiu, *Environ. Sci. Technol.*, 2008, **42**, 6955–6960.
13 B. Qiu, C. Xu, D. Sun, H. Wei, X. Zhang, J. Guo, Q. Wang, D. Rutman, Z. Guo and S. Wei, *RSC Adv.*, 2014, **4**, 29855–29865.
14 Z. Feng, S. Zhu, D. R. M. de Godoi, A. C. S. Samia and D. Scherson, *Anal. Chem.*, 2012, **84**, 3764–3770.
15 W. Luo, L. Zhu, N. Wang, H. Tang, M. Cao and Y. She, *Environ. Sci. Technol.*, 2010, **44**, 1786–1791.
16 L.-N. Shi, X. Zhang and Z.-L. Chen, *Water Res.*, 2011, **45**, 886–892.
17 M. Bhaumik, A. Maity, V. V. Srinivasu and M. S. Onyango, *J. Hazard. Mater.*, 2011, **190**, 381–390.
18 E.-J. Kim, C.-S. Lee, Y.-Y. Chang and Y.-S. Chang, *ACS Appl. Mater. Interfaces*, 2013, **5**, 9628–9634.
19 X. Liu, Q. Hu, Z. Fang, X. Zhang and B. Zhang, *Langmuir*, 2008, **25**, 3–8.
20 W. Liu, J. Zhang, C. Zhang and L. Ren, *Chem. Eng. J.*, 2012, **189–190**, 295–302.
21 J. Zhu, H. Gu, J. Guo, M. Chen, H. Wei, Z. Luo, H. A. Colorado, N. Yerra, D. Ding, T. C. Ho, N. Haldolaarachchige, J. Hopper, D. P. Young, Z. Guo and S. Wei, *J. Mater. Chem. A*, 2014, **2**, 2256–2265.
22 Y. Zhai, Y. Dou, X. Liu, B. Tu and D. Zhao, *J. Mater. Chem.*, 2009, **19**, 3292–3300.
23 W. Gao, Y. Wan, Y. Dou and D. Zhao, *Adv. Energy Mater.*, 2011, **1**, 115–123.
24 W. Wang, H.-Y. Wang, W. Wei, Z.-G. Xiao and Y. Wan, *Chem.–Eur. J*, 2011, **17**, 13461–13472.
25 T. Madrakian, A. Afkhami, M. Ahmadi and H. Bagheri, *J. Hazard. Mater.*, 2011, **196**, 109–114.
26 J. Zhu, S. Wei, H. Gu, S. B. Rapole, Q. Wang, Z. Luo, N. Haldolaarachchige, D. P. Young and Z. Guo, *Environ. Sci. Technol.*, 2012, **46**, 977–985.
27 V. Chandra, J. Park, Y. Chun, J. W. Lee, I.-C. Hwang and K. S. Kim, *ACS Nano*, 2010, **4**, 3979–3986.
28 C. Chen, P. Gunawan and R. Xu, *J. Mater. Chem.*, 2011, **21**, 1218–1225.
29 G. Xie, P. Xi, H. Liu, F. Chen, L. Huang, Y. Shi, F. Hou, Z. Zeng, C. Shao and J. Wang, *J. Mater. Chem.*, 2012, **22**, 1033–1039.
30 C. Wang, C. Feng, Y. Gao, X. Ma, Q. Wu and Z. Wang, *Chem. Eng. J.*, 2011, **173**, 92–97.
31 L. Ai, C. Zhang and Z. Chen, *J. Hazard. Mater.*, 2011, **192**, 1515–1524.
32 J. Zhan, I. Kolesnichenko, B. Sunkara, J. He, G. L. McPherson, G. Piringer and V. T. John, *Environ. Sci. Technol.*, 2011, **45**, 1949–1954.
33 S. A. Johnson, E. S. Brigham, P. J. Ollivier and T. E. Mallouk, *Chem. Mater.*, 1997, **9**, 2448–2458.
34 J. Rodriguez-Mirasol, T. Cordero, L. R. Radovic and J. J. Rodriguez, *Chem. Mater.*, 1998, **10**, 550–558.
35 Y. Zhai, Y. Dou, D. Zhao, P. F. Fulvio, R. T. Mayes and S. Dai, *Adv. Mater.*, 2011, **23**, 4828–4850.
36 J. S. Lee, A. Hirao and S. Nakahama, *Macromolecules*, 1988, **21**, 274–276.
37 M. Templin, A. Franck, A. Du Chesne, H. Leist, Y. Zhang, R. Ulrich, V. Schädler and U. Wiesner, *Science*, 1997, **278**, 1795–1798.
38 Y. Wan, X. Cui and Z. Wen, *J. Hazard. Mater.*, 2011, **198**, 216–223.
39 S. Glatzel, Z. Schnepp and C. Giordano, *Angew. Chem., Int. Ed.*, 2013, **52**, 2355–2358.
40 S. H. Park, S. M. Jo, D. Y. Kim, W. S. Lee and B. C. Kim, *Synth. Met.*, 2005, **150**, 265–270.
41 J. Zhu, S. Wei, Y. Li, S. Pallavkar, H. Lin, N. Haldolaarachchige, Z. Luo, D. P. Young and Z. Guo, *J. Mater. Chem.*, 2011, **21**, 16239–16246.
42 J. Zhu, S. Pallavkar, M. Chen, N. Yerra, Z. Luo, H. A. Colorado, H. Lin, N. Haldolaarachchige, A. Khasanov, T. C. Ho, D. P. Young, S. Wei and Z. Guo, *Chem. Commun.*, 2013, **49**, 258–260.
43 Z. Liu, J. Wang, V. Kushvaha, S. Poyraz, H. Tippur, S. Park, M. Kim, Y. Liu, J. Bar, H. Chen and X. Zhang, *Chem. Commun.*, 2011, **47**, 9912–9914.
44 J. Maire and J. Mering, in *Chem. Phys. Carbon*, ed. P. L. Walker and J. A. Thrower, Dekker, New York, 1971, vol. 6, pp. 125–190.
45 Y. Zhai, Y. Dou, X. Liu, B. Tu and D. Zhao, *J. Mater. Chem.*, 2009, **19**, 3292–3300.
46 P. F. Fulvio, R. T. Mayes, X. Wang, S. M. Mahurin, J. C. Bauer, V. Presser, J. McDonough, Y. Gogotsi and S. Dai, *Adv. Funct. Mater.*, 2011, **21**, 2208–2215.
47 N. Ahmed El, *J. Hazard. Mater.*, 2009, **161**, 132–141.
48 J. Zhu, H. Gu, S. B. Rapole, Z. Luo, S. Pallavkar, N. Haldolaarachchige, T. J. Benson, T. C. Ho, J. Hopper, D. P. Young, S. Wei and Z. Guo, *RSC Adv.*, 2012, **2**, 4844–4856.
49 L.-S. Zhong, J.-S. Hu, A.-M. Cao, Q. Liu, W.-G. Song and L.-J. Wan, *Chem. Mater.*, 2007, **19**, 1648–1655.
50 A. K. Bhattacharya, T. K. Naiya, S. N. Mandal and S. K. Das, *Chem. Eng. J.*, 2008, **137**, 529–541.
51 Y. S. Ho, G. McKay, D. A. J. Wase and C. F. Forster, *Adsorpt. Sci. Technol.*, 2000, **18**, 639–650.

52 R.-S. Juang and M.-L. Chen, *Ind. Eng. Chem. Res.*, 1997, **36**, 813–820.
53 Kinetics of Reaction in Pure and Mixed Systems, in *Soil Physical Chemistry*, ed. D. L. Sparks, CRC press, Boca Raton, 1986.
54 S. K. Srivastava, R. Tyagi and N. Pant, *Water Res.*, 1989, **23**, 1161–1165.
55 A. El-Sikaily, A. E. Nemr, A. Khaled and O. Abdelwehab, *J. Hazard. Mater.*, 2007, **148**, 216–228.